

Dissociative recombination of rotationally cold ArH⁺

Ábel Kálosi ^{1,2,*}, Manfred Grieser ², Leonard W. Isberner,^{2,3} Holger Kreckel ², Åsa Larson ⁴, David A. Neufeld ⁵,
Ann E. Orel ⁶, Daniel Paul ^{1,2}, Daniel W. Savin ¹, Stefan Schippers ³, Viviane C. Schmidt ², Andreas Wolf ²,
Mark G. Wolfire,⁷ and Oldřich Novotný ²

¹*Columbia Astrophysics Laboratory, Columbia University, New York, New York 10027, USA*

²*Max-Planck-Institut für Kernphysik, Saupfercheckweg 1, D-69117 Heidelberg, Germany*

³*I. Physikalisches Institut, Justus-Liebig-Universität Gießen, D-35392 Gießen, Germany*

⁴*Department of Physics, Stockholm University, AlbaNova University Center, SE-106 91 Stockholm, Sweden*

⁵*Department of Physics & Astronomy, Johns Hopkins University, Baltimore, Maryland 21218, USA*

⁶*Department of Chemical Engineering, University of California, Davis, California 95616, USA*

⁷*Department of Astronomy, University of Maryland, College Park, Maryland 20742, USA*



(Received 16 May 2024; accepted 26 July 2024; published 22 August 2024)

We have experimentally studied dissociative recombination (DR) of electronically and vibrationally relaxed ArH⁺ in its lowest rotational levels, using an electron-ion merged-beams setup at the Cryogenic Storage Ring. We report measurements for the merged-beams rate coefficient of ArH⁺ and compare it to published experimental and theoretical results. In addition, by measuring the kinetic energy released to the DR fragments, we have determined the internal state of the DR products after dissociation. At low collision energies, we find that the atomic products are in their respective ground states, which are only accessible via nonadiabatic couplings to neutral Rydberg states. Published theoretical results for ArH⁺ have not included this DR pathway. From our measurements, we have also derived a kinetic temperature rate coefficient for use in astrochemical models.

DOI: [10.1103/PhysRevA.110.022816](https://doi.org/10.1103/PhysRevA.110.022816)

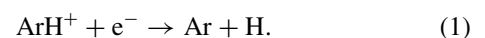
I. INTRODUCTION

Dissociative recombination (DR) with free electrons is an important neutralization process for molecular cations in a variety of laboratory, industrial, and astrophysical environments [1]. Historically, DR was proposed to proceed via electron capture into a neutral dissociative (resonance) state with a potential energy curve (PEC) that crosses the PEC of the target ion. It was soon recognized that the incoming electron could also be captured into a ro-vibrationally excited Rydberg state, forming an intermediate step that then predissociates via a suitable state. These two pathways were dubbed the direct and indirect DR mechanisms [2,3] and are illustrated schematically in Fig. 1. Both mechanisms occur simultaneously and interference between them will cause sharp structures observed in high-resolution cross-section measurements. Since the two mechanisms cannot be separated, modern theories strive either to improve the existing unified treatments or to elaborate new ones that are more generally applicable or accurate (e.g., Ref. [4] and references therein).

In some systems, though, direct DR is significantly suppressed. Either there is no electronic resonant state with a

PEC crossing the ionic PEC, or the resonant state PEC does not cross the ionic PEC close to its equilibrium internuclear distance, the latter of which is illustrated schematically in Fig. 1. Instead, electron capture at low energies is driven by recombination into a rovibrationally excited Rydberg state of the neutral molecule. This Rydberg state predissociates by nonadiabatic couplings to a state that is open for dissociation [5]. This mechanism is illustrated with the blue arrows in Fig. 1 and occurs for certain rare gas diatomic hydrides [6–8]. Direct DR is negligible in these systems at low collision energies. To theoretically model the indirect DR process, reliable descriptions are needed for the nonadiabatic couplings among the series of infinite numbers of bound Rydberg states, as well as the coupling to the ionization continuum. Recent multichannel quantum defect theory (MQDT) calculations on the relatively simple HeH⁺ system [8] have highlighted the importance of using an optimal origin for the coordinate system in which the quantum defects of the Rydberg states are calculated. These calculations also predicted a considerable influence of the rotational structure on the DR cross section. This had already been observed experimentally in rotational-level-resolved DR measurements for HeH⁺ that were enabled by recent laboratory advances [9]. Good agreement between theory and experiment for this simple system was achieved for cross sections at collision energies as low as a few meV [8].

Here, we move to a theoretically more challenging system with a higher level of electronic complexity and report laboratory measurements for DR of ground state ArH⁺, which can be schematically represented as



*Contact author: abel.kalosi@outlook.com

Published by the American Physical Society under the terms of the [Creative Commons Attribution 4.0 International](https://creativecommons.org/licenses/by/4.0/) license. Further distribution of this work must maintain attribution to the author(s) and the published article's title, journal citation, and DOI. Open access publication funded by Max Planck Society.

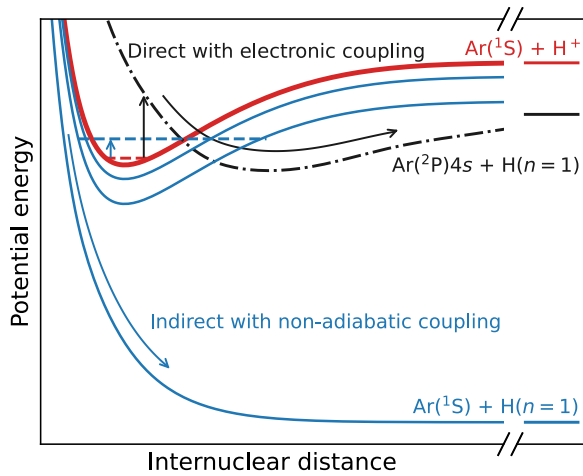


FIG. 1. Schematic PECs illustrating some of the possible DR mechanisms of ArH^+ at low and high collision energies, shown by the short blue and long black arrow pairs, respectively. The thick red curve is the PEC of the target ion. Below the ionic PEC are Rydberg PECs of the neutral system, which have similar shapes to the ionic PEC. For clarity, only two of the infinite number of Rydberg PECs are shown by thin blue curves. The horizontal dashed lines highlight selected rovibrational levels of the ionic and Rydberg PECs to which they are connected. At low collision energies, the electron is captured into a rovibrationally excited Rydberg state. The system then predissociates through nonadiabatic couplings to the ground state (left-side blue pathway). At higher collision energies, the electron can be captured into an electronic resonant state, shown by the dotted-dashed black curve, that leads directly to dissociation (right-side black pathway). On the right-hand side of the figure, the horizontal full lines show the dissociation limits for the neutral and ionic ground states and the electronic resonant state, shown by the blue, red, and black, respectively.

The only published experimental data are the results of a merged-beams experiment from the room-temperature ASTRID storage ring [7]. However, their measurements could only put an upper limit on the strength of the DR process at collision energies $\lesssim 1$ eV, where the indirect process is expected to dominate in ArH^+ .

To the best of our knowledge, no published theoretical calculations are available for low-energy DR of ArH^+ . Recent theoretical MQDT calculations included dissociation through several resonance states of ArH that cross the ionic ground-state PEC at internuclear distances much larger than the equilibrium distance of ArH^+ [10,11]. Given that the resonance states considered correlate with dissociation limits located above the ionic ground vibrational level, the calculated DR cross section is only nonzero when these channels become energetically open ($\gtrsim 1$ eV) [10,11].

Renewed interest in DR of ArH^+ is also linked to its astrophysical application. $^{36}\text{ArH}^+$ was the first noble gas molecule to be detected in interstellar space [12], where it was seen in emission. Subsequently, two isotopologues, $^{36}\text{ArH}^+$ and $^{38}\text{ArH}^+$, were observed in absorption in astronomical spectra [13,14], showing that ArH^+ can be produced in a variety of environments, ranging from diffuse clouds to supernova remnants. The relatively low DR rate coefficient of ArH^+ is expected to contribute to its survival at conditions where

most other diatomic species would be destroyed at rates more than two orders of magnitude faster. Recent astrochemical models have adopted the upper limit of the room-temperature ASTRID measurements over a wide range of temperatures [15,16], leading to two potential complications. In interstellar clouds, where collisional timescales are much longer than radiative lifetimes, only the lowest rotational level of ArH^+ is populated, and state-specific data are needed. In environments with kinetic temperatures of ~ 1000 K, a reliable temperature dependence is needed. In both instances, the ASTRID results do not accommodate the needs of the astronomical community.

Our work here addresses both the molecular physics and astrophysics issues related to DR of ArH^+ . The remainder of this paper is structured as follows. In Sec. II, we briefly discuss the experimental setup and data analysis. In Sec. III, we present the measured merged-beams rate coefficient, fragment-imaging results, and the derived kinetic temperature rate coefficient for plasma applications. In Sec. IV, calculated potential energy curves of the ArH and ArH^+ systems relevant for the low-energy DR are presented. In Sec. V, the present results are discussed in the context of DR theory and astrochemistry. A summary is given in Sec. VI.

II. EXPERIMENTAL DESCRIPTION

DR measurements were performed on internally cold $^{40}\text{ArH}^+$ using the Cryogenic Storage Ring (CSR) [17] facility at the Max Planck Institute for Nuclear Physics in Heidelberg, Germany. We followed the methodology of our earlier measurements to determine the merged-beams rate coefficient and to perform imaging of the DR products [9,18,19]. Here we discuss only those new aspects specific to the present measurements.

A. Ion beam and storage

$^{40}\text{ArH}^+$ ions were generated in an electron cyclotron resonance (ECR) ion source, using argon buffer gas with a few percent admixture of hydrogen. A current of up to a few hundred nA was extracted, accelerated to an energy of ≈ 300 keV, mass-to-charge selected using a series of dipole magnets, and then injected into CSR. We typically injected around 1×10^7 ions, in order to remain within the linear counting regime of our neutral particle detector. The injected ions were stored on a closed orbit in CSR and merged with a magnetically confined electron beam in the electron cooler straight section of the ring. The storage ring lattice was set up in the so-called achromat mode, a configuration where the momentum dispersion was near zero in the electron-ion overlap section. This mode was necessary for efficient phase-space cooling of the ArH^+ ion beam, also known as electron cooling [20]. Electron cooling enables us to reduce the diameter and energy spread of the stored ion beam. We typically observed exponential beam lifetimes of > 600 s for electron-cooled beams. For data collection, we stored the ions for times of up to 450 s.

Gas-discharge ion sources produce internally excited ions. Once the ions were stored, they rapidly relaxed to their ground electronic and vibrational states, within a few ms after

injection. Rotational relaxation was driven by spontaneous emission in the cryogenic black-body environment of CSR [21–23] on timescales of tens of seconds. Additionally, the stored ions benefited from rotational cooling through electron-ion rotational-level-changing collisions using the electron beam. A much colder rotational distribution was reached than that of the ASTRID ArH⁺ study [7]. Using our collisional-radiative model for the populations of rotational levels [23], labeled by quantum number J for ArH⁺, we estimate that $\approx 57\%$ of the ions were in the $J = 0$ ground level, $\approx 37\%$ in the $J = 1$ level, and $\approx 6\%$ in the $J = 2$ level during data collection for DR (see Appendix A).

We used a high-purity beam of ⁴⁰ArH⁺ that was monitored *in situ* during ion storage. The initial beam purity was verified by operating CSR in the recently developed isochronous mode, i.e., as a time-of-flight mass spectrometer with a mass resolution of $\sim 10^{-5}$ u [24]. A particular concern was contamination by potential impurities in the ion source discharge, namely, ¹²C₃H₅⁺ and ¹²CH₃CN⁺, which differ in mass from ⁴⁰ArH⁺ by $\approx 7 \times 10^{-2}$ u and $\approx 6 \times 10^{-2}$ u, respectively. To enhance the purity of the stored beam, we used the electron beam to deplete these impurities, which have orders of magnitude higher DR rate coefficients compared to ArH⁺. Using the imaging techniques introduced in Appendix B, a detailed contaminant analysis is given in Appendix C.

B. Merged-beams experiment

DR measurements were performed using an electron-ion merged-beams configuration that has been discussed in detail elsewhere [9,18,19]. In the present measurements, the relative collision energy between the merged beams was controlled by varying the voltage on a set of biased drift tubes in the electron cooler. This enabled us to tune the nominal laboratory-frame electron-beam energy in the interaction region E_e . The drift tubes define the effective interaction region of the merged-beams setup. DR reactions produced neutral fragments [see Reaction (1)] that retained nearly the same laboratory-frame velocity as the reacting ion and continued on ballistic trajectories. The neutral reaction products were collected by a particle-counting and impact-position-imaging detector that was located 3.8 m downstream of the electron-ion interaction region and oriented to face perpendicular to the beam direction. By recording the count rate of DR reactions as a function of the relative electron-ion collision velocity v_r , we measured the merged-beams rate coefficient

$$\alpha^{\text{mb}} = \langle \sigma v_r \rangle, \quad (2)$$

where the product of v_r and the energy-dependent DR cross section σ is averaged over the velocity distribution in the electron-ion overlap section. The main experimental factors determining the velocity distribution are the perpendicular and parallel temperature components T_{\perp} and T_{\parallel} , respectively, in the frame of the bulk electron-velocity vector; the merging and demerging geometry; and the variable laboratory-frame energy of the electrons E_e . We modeled the velocity distribution following our previous approaches [23,25]. Additionally, it is practical to express the collision-energy distribution as a function of the detuning energy E_d , defined as the nominal

TABLE I. Reaction threshold energies E_r according to Eq. (8) for the four lowest excited-state products for DR of ground state ArH⁺. The reaction energies for Ar excited states are calculated as the weighted average of the J sublevel energies.

Ar	H	E_r (eV)
[Ne]3s ² 3p ⁶ (¹ S)	$n = 2$	0.5
[Ne]3s ² 3p ⁵ (² P _{3/2} ^o)4s	$n = 1$	1.9
[Ne]3s ² 3p ⁵ (² P _{1/2} ^o)4s	$n = 1$	2.1
[Ne]3s ² 3p ⁶ (¹ S)	$n = 3$	2.4

center-of-mass collision energy,

$$E_d = (\sqrt{E_e} - \sqrt{E_0})^2, \quad (3)$$

where E_0 is the laboratory-frame electron-beam energy at matched electron-ion velocities, substituting the reduced mass of the collision system by that of the electron.

For the present measurements, we used a magnetically confined electron beam with a current of 9.15 μ A and a circular density profile that was nearly uniform. The initial laboratory-frame energy of the electrons, ≈ 7 eV, was chosen so that the merging-geometry-dependent collision energies outside the effective interaction region were $\lesssim 0.5$ eV, i.e., below the first excited DR product threshold (see Table I). The electrons were guided into CSR by a stepwise reduction in magnetic field strength, decreasing to 10 mT in the interaction region. The total adiabatic expansion factor was 30, resulting in an expanded beam diameter of 12.1 ± 0.6 mm. For the perpendicular electron-beam temperature, we take $k_B T_{\perp} = 2.0 \pm 1.0$ meV [26]. The parallel electron-beam temperature is energy dependent [27], with a value of $k_B T_{\parallel} \approx 0.26$ meV at matched velocities.

Electron cooling occurs for matched electron-ion velocities and was utilized for all DR measurements. Using Schottky pickup observations [17], we measured the revolution frequency and momentum spread of the stored ions. The corresponding laboratory-frame electron-beam energy was $E_0 = 4.003 \pm 0.012$ eV at matched velocities, also called the cooling energy. For the DR measurements, we applied uninterrupted electron cooling immediately after ion injection, for a duration of 42 s. This resulted in the reduction of the injected ion-beam horizontal and vertical full width at half-maxima (FWHM) to $<5.2 \pm 0.7$ mm and $<2.8 \pm 0.5$ mm, respectively.

Measurements of the collision-energy-dependent merged-beams rate coefficient were performed as a function of storage time, starting at 42 s after ion injection, by periodically detuning the electron-beam energy E_e from matched velocities. The measurements were grouped into predefined sets of E_d values. Data were collected for 25 ms at a given measurement E_d , followed by electron cooling for 100 ms, a reference energy of $E_d = 30$ eV for 25 ms, and electrons off for 25 ms. We also included an ~ 5 ms waiting time between each of these steps for the system to stabilize.

The measured absolute merged-beams rate coefficient,

$$\alpha^{\text{mb}}(E_d) = \frac{R_e(E_d)}{\eta(E_d)\xi N_i n_e(E_d)\hat{I}_0/C_0}, \quad (4)$$

is directly proportional to the electron-induced count rate $R_e(E_d)$. At most energies $R_e(E_d)$ is due to DR. Above 3.9 eV, it may be partly also due to dissociative excitation (DE). Quantities that are energy dependent, such as the detection efficiency for DR events $\eta(E_d)$ and the electron density $n_e(E_d)$, are discussed below. The fraction of ions enclosed by the electron beam in the effective interaction region, $\xi > 0.992$, was determined from the profiles of the ion and electron beams. N_i is the number of stored ions. The effective electron-ion overlap length is measurement specific; here $\hat{l}_0 = 0.79 \pm 0.01$ m. It has been previously defined in Ref. [23]. The circumference of the ion-beam orbit is $C_0 = 35.12 \pm 0.05$ m.

Additional background processes, due to residual-gas-induced collisions and the intrinsic dark rate of the neutral detector, contribute to the measured count rate during a DR measurement step. $R_e(E_d)$ was determined after subtracting the count rate due to background contributions measured in the corresponding electrons-off step.

We determined $\eta(E_d)$ by comparing single- and double-particle hits on the detector [18]. Due to the finite size of the particle-counting detector, $\eta(E_d)$ is dependent on the kinetic energy released (KER) in the DR process and the branching ratios between dissociation channels. For additional details see Appendix B. At matched velocities, we obtained $\eta(0 \text{ eV}) = 0.62$ and applied this value for all $E_d < 1.85$ eV. Above this energy, the $\text{Ar}^{(2P)4s} + \text{H}(n=1)$ DR channels open and dominate the measured particle flux (see Sec. III B). We analyzed $\eta(E_d)$ at selected energies from 3 to 7.5 eV and found values that decreased monotonically from 0.87 to 0.65. We constructed a geometrical detector-cutoff model, assuming an isotropic transverse fragment distribution [19] and taking into account the increase of the KER with E_d , to find a smooth representation for $\eta(E_d)$ from 1.85 to 7 eV. Above 7 eV, we used a single effective value of 0.64.

Equation (4) was initially evaluated on a relative scale by replacing the storage-time-dependent ion number $N_i(t)$ with an electron-induced neutralization signal. In specific, we normalized using the count rate at the reference energy of $E_d = 30$ eV, $R_{\text{ref}}(t)$, determined from the reference rate minus the electrons-off rate. R_{ref} was measured at a sufficiently high energy that the neutralization rate coefficient can be assumed to be independent of the internal state of the ions. The $\alpha^{\text{mb}}(E_d)$ measurements were accompanied by a calibration of $R_{\text{ref}}(t)$ to $N_i(t)$, expressed as a proportionality factor $S_b = R_{\text{ref}}(t)/N_i(t)$. N_i was measured using beam bunching combined with a capacitive current pickup (PU-C in Ref. [17]). The absolute current measurement for PU-C was calibrated with a 10% systematic uncertainty [18]. The determined S_b is specific to the present ArH^+ campaign as it is proportional to the electron density and the neutralization rate coefficient for ArH^+ at $E_d = 30$ eV. To verify the linear behavior of S_b , we used ion-beam bunching at various storage times and for ion numbers in the range of 3×10^6 to 1.2×10^7 . The uncertainty due to beam bunching introduced an additional 15% uncertainty when evaluating S_b .

The $\alpha^{\text{mb}}(E_d)$ measurements were performed using a constant electron current. Combined with the measured electron-beam radius, we determined the energy dependent $n_e(E_d)$ by taking into account the laboratory-frame electron energy versus E_d . The measurement value at matched velocities was

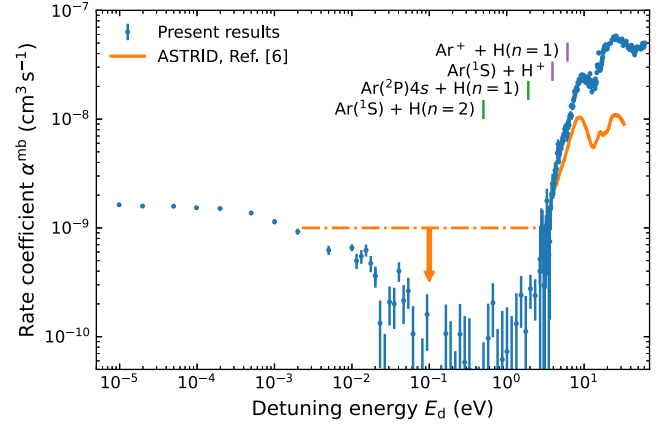


FIG. 2. Measured merged-beams rate coefficient α^{mb} for neutralization of ArH^+ ions in collisions with electrons vs detuning energy E_d . The present results are plotted as blue symbols with error bars representing one-sigma statistical uncertainties. The absolute scaling of the results has a systematic accuracy of 21% at $E_d \leq 7$ eV. Also shown are the results from the room-temperature ASTRID study, indicated by the full orange line [7]. The ASTRID data are plotted only for values above $1 \times 10^{-9} \text{ cm}^3 \text{ s}^{-1}$, the corresponding low-energy results are represented by the horizontal dotted-dashed line. The vertical lines with labels highlight reaction threshold energies E_r for selected DR and DE products. Our measured α^{mb} is provided in tabulated form in Ref. [28].

$n_e(0 \text{ eV}) = (4.2 \pm 0.4) \times 10^5 \text{ cm}^{-3}$. The total systematic uncertainty of the absolute scaling for our merged-beams DR rate coefficient α^{mb} was determined by adding all contributing uncertainties listed above in quadrature. The resulting total systematic uncertainty of 21% is valid for $E_d < 7$ eV.

The particle-counting detector used in this study is also capable of imaging the impact positions and measuring the temporal separation of the neutral DR fragments. The 120-mm-diameter microchannel plate (MCP) detector was backed by a phosphor anode that converted the electron cascade signal from the MCP into light spots, signifying the impact positions, that were observed with an optical camera. The particle detection electronics were triggered by a silicon photomultiplier that viewed the phosphor screen and was used to synchronize the optical camera and electronic readout systems. Impact positions were read out by a 1-kHz frame-rate optical camera, with an exposure time of $\approx 2 \mu\text{s}$. Arrival times were determined by analyzing the MCP electronics signal. Additional details about the imaging setup can be found in Ref. [27]. For DR, the typical temporal separation between the Ar and H fragments was < 150 ns. By measuring the distance and time between the fragments, we generated three-dimensional (3D) images of the dissociating fragments. From these data we determined the KER in the DR process and identified the internal state of the products after dissociation.

III. EXPERIMENTAL RESULTS

A. Merged-beams rate coefficient

The measured merged-beams rate coefficient $\alpha^{\text{mb}}(E_d)$ for reactive collisions of ArH^+ with electrons is plotted in Fig. 2. We first compare our results with those measured at the

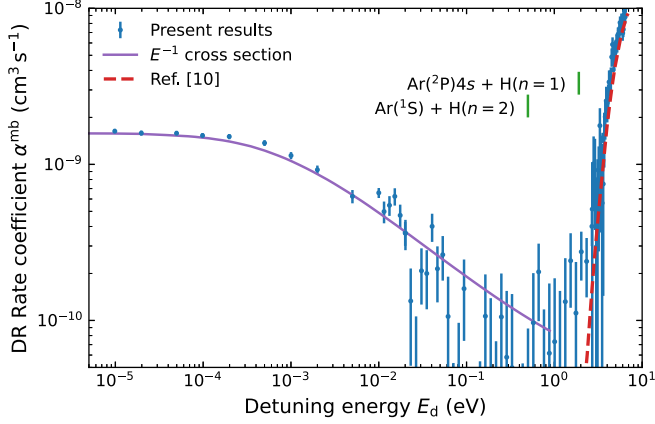


FIG. 3. Same as Fig. 2 but comparing with two different theoretical cross-section models. The theoretical results have been transformed into a merged-beams rate coefficient using our collision velocity distribution.

room-temperature ASTRID storage ring [7]. At the lowest resolved energies ($\sim 10^{-3}$ eV), no measurable signal was detected in the ASTRID measurements and an upper limit of 1×10^{-9} $\text{cm}^3 \text{s}^{-1}$ was determined [7]. In our measurements, α^{mb} is approximately constant below 10^{-3} eV, as expected for our energy resolution. Between 0.1 and 1 eV, the CSR values are almost an order of magnitude lower than the low-energy limit of the ASTRID data. Here, our statistical counting uncertainties vary from 0.9×10^{-10} to 1.1×10^{-10} $\text{cm}^3 \text{s}^{-1}$. By calculating an energy-independent mean from the CSR DR signal rate between 0.1 and 1 eV, we derive a limit of $(0.6 \pm 2.4) \times 10^{-11}$ $\text{cm}^3 \text{s}^{-1}$, which is a more than an order of magnitude improvement over the ASTRID limit.

At energies > 3.9 eV, DE has to be considered as an additional process that results in neutral fragments and can contribute to the measured signals. The CSR particle detection system is currently not capable of distinguishing between DR and DE, while the ASTRID experiments used a mass-sensitive detection method that could distinguish between DR and those DE events that result in the production of only neutral H [7]. Still, both measurements potentially included the DE channel



which is energetically accessible for collision energies above 3.9 eV.

Between ≈ 3 and 6 eV, we find reasonable agreement between the shape of the CSR and ASTRID DR results, taking into account the uncertainty in the absolute scaling of the ASTRID measurements. Above ≈ 6 eV, the CSR and ASTRID results gradually diverge. We attribute this to the opening of the DE channel



which has a threshold of 6.1 eV and could be discriminated against in the ASTRID results.

A comparison of the measured DR rate coefficient $\alpha^{\text{mb}}(E_d)$ with two different models is plotted in Fig. 3. The cross sections were converted into α^{mb} using our collision velocity distribution. For $E_d < 1$ eV we used a structureless

cross-section model given by a collision energy dependence of E^{-1} and scaled to the measured data at matched velocities. This model represents electron capture without taking into account the internal structure of the target ion or any relevant intermediate states [3]. For $E_d \gtrsim 2$ eV, we can compare to the theoretical calculations of Refs. [10,11], which show good agreement with our experimental results, to within our systematic uncertainty of 21%. This suggests that the DE channels of Eqs. (5) and (6) contribute at most at the level of the systematic uncertainty in the measured α^{mb} for E_d between 3.9 and 6.0 eV.

B. 3D imaging

We determined the internal state of the DR products using the energy E_{KER} of the DR fragments. For this, we acquired 3D imaging data from the measured impact distances and temporal separations. Dedicated measurements were performed for several values of E_d . To account for the finite electron-ion overlap length, the results are presented as effective $E_{\text{KER}}^{\text{eff}}$ distributions. Details are provided in Appendix B. Here, we focus on the interpretation of the measurements.

The internal states for the DR products are identified using conservation of energy. For ArH^+ , E_{KER} can be predicted from known atomic and molecular properties as

$$E_{\text{KER}} = E_I(\text{H}) - D_0(\text{ArH}^+) - E(\text{Ar}) - E(\text{H}) + E(\text{ArH}^+) + E_c, \quad (7)$$

where $E_I(\text{H})$ is the ionization energy of H; $D_0(\text{ArH}^+)$ is the dissociation energy of ground state ArH^+ ; $E(\text{Ar})$, $E(\text{H})$, and $E(\text{ArH}^+)$ are the respective internal excitation energies of Ar, H, and ArH^+ , relative to their ground levels; and E_c is the collision energy. For a nominal $E_c = 0$ eV, DR of ground state $\text{ArH}^+ \text{X}^1\Sigma^+(v=0, J=0)$ producing ground state $\text{Ar}(^1S)$ and $\text{H}(n=1)$ results in an expected $E_{\text{KER}} = 9.7$ eV. For all excited atomic states at a nominal $E_c = 0$ eV, the calculated E_{KER} results in negative values. This indicates that those states can only be reached when additional collision energy or internal energy of ArH^+ are added into the system. For ground state ArH^+ , it is useful to express the threshold for the formation of specific final states as the reaction energy

$$E_r = D_0(\text{ArH}^+) + E(\text{Ar}) + E(\text{H}) - E_I(\text{H}). \quad (8)$$

Table I lists the four lowest excited-product-state combinations relevant for our measurements.

The measured $E_{\text{KER}}^{\text{eff}}$ distribution for DR at matched velocities ($E_d = 0$ eV) is plotted in Fig. 4. The data are shown for orientation angles of $\vartheta < 20^\circ$ and $\vartheta > 160^\circ$. These angles represent orientations of the internuclear axis, relative to the bulk electron-ion velocity vector, for which the particle detector can collect all fragments, independent of either E_{KER} or the distance from the dissociation location to the detector. Under these conditions, we can compare our data with the empirical model given by Eq. (B5). By using an effective interaction length of $\Delta L = 0.79$ m, and parameters δ and I determined by least-squares fitting, we can reproduce well the observed data for an $E_{\text{KER}} = 9.7$ eV expected for $\text{Ar}(^1S) + \text{H}(n=1)$.

We also measured $E_{\text{KER}}^{\text{eff}}$ distributions for DR at collisions energies between 2 to 3 eV, at which several of the excited

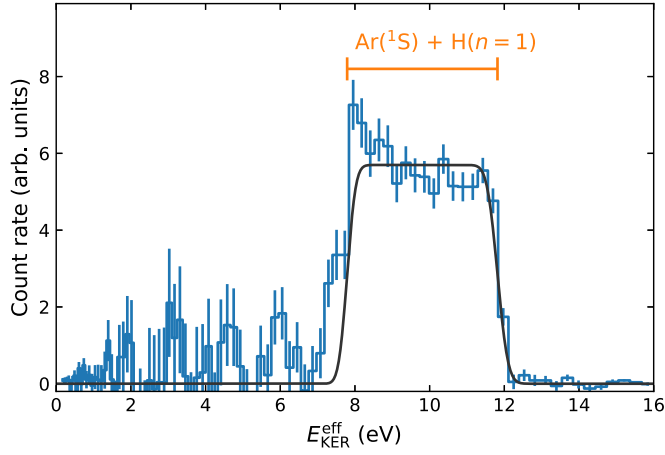


FIG. 4. Measured $E_{\text{KER}}^{\text{eff}}$ distribution for DR of stored ArH^+ ions at matched velocities ($E_d = 0$ eV). The electron-induced signal is plotted in arbitrary units vs $E_{\text{KER}}^{\text{eff}}$. The results are shown, for events with $\vartheta < 20^\circ$ and $\vartheta > 160^\circ$, as the histogram with one-sigma statistical counting uncertainties. The horizontal orange line with vertical bars is labeled by the DR product states for Ar and H. It shows the range where signal corresponds to $E_{\text{KER}} = 9.7$ eV and an effective interaction length of $\Delta L = 0.79$ m. The black full line shows the modeled distribution using Eq. (B5).

product states given in Table I are energetically accessible. The data are plotted in Fig. 5 without restrictions on ϑ in order to enable the highest sensitivity for weak signals. According to the calculations of Refs. [10,11], Ar states with an electron excited to the $4s$ orbital are expected to be the dominant products for DR at these energies. This has been confirmed in our data for $E_d = 3$ eV. We also aimed to detect if any of the other energetically accessible states listed in Table I were produced. However, we found no signal within the statistical quality of the data.

C. Kinetic rate coefficient

For use in chemical models, we have generated a kinetic-temperature-dependent rate coefficient $\alpha^k(T_k)$ from our $\alpha^{\text{mb}}(E_d)$ results, following the DR cross-section-extraction method from our previous work [18,25]. Here, T_k is the kinetic temperature of the gas, which characterizes the Maxwell-Boltzmann velocity distribution for all particles. We have determined α^k from $T_k = 10$ to 20 000 K, as plotted in Fig. 6. For this temperature range, the possible contributions of DE, as discussed previously, have no impact on our α^k . We provide fitting formulas for the rate coefficient in Appendix D. The total systematic uncertainty of α^k at most temperatures is due to the absolute scaling of α^{mb} and the uncertainty of T_\perp ; however, around the minimum of α^k , the statistical counting uncertainty contributes as well. To determine the lower error band in the cross-section-extraction procedure, we have set to zero all α^{mb} values for which the statistical counting uncertainty exceeds the measured value. Also shown in the figure are the experimentally derived upper limit used in astrochemical models [13] and the theoretical DR results of Refs. [10,11].

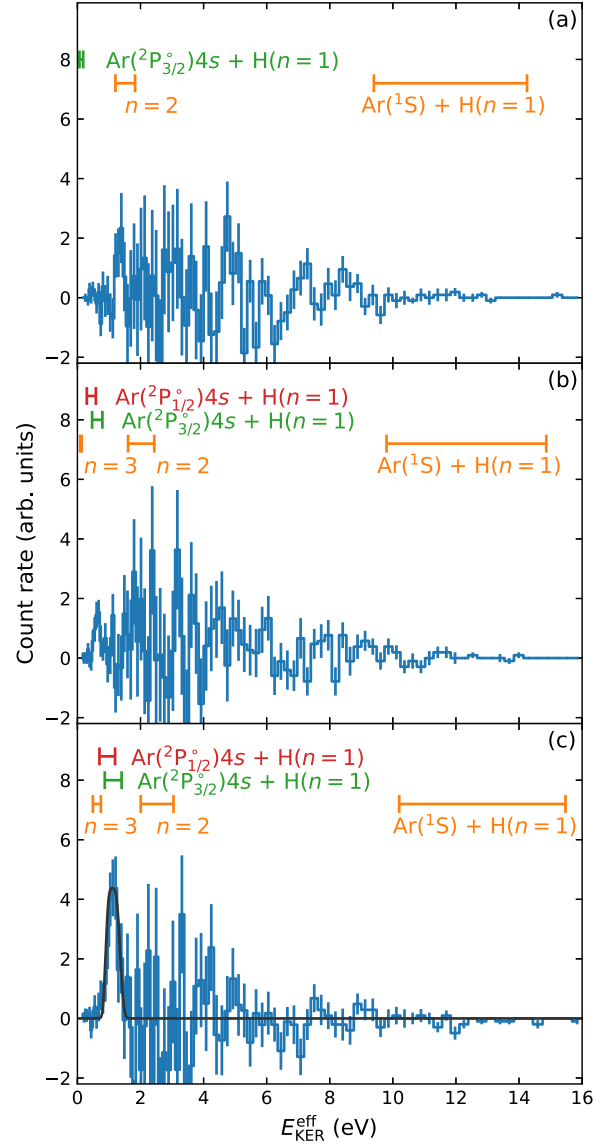


FIG. 5. Same as Fig. 4 but for all values of ϑ and three values of E_d above the 1.9-eV excitation threshold for the production of excited Ar final states. The horizontal lines with vertical bars are labeled by the various DR product states for Ar and H. They show the energy ranges where signal would correspond to the possible product channels and an effective interaction length of $\Delta L = 0.79$ m. Data are shown for (a) $E_d = 2$ eV, (b) 2.5 eV, and (c) 3 eV. The black full line in (c) shows the modeled distribution using Eq. (B5) for $E_{\text{KER}} = 1.1$ eV.

IV. THEORETICAL DESCRIPTION

To theoretically describe the electronic states relevant for DR, it is crucial to have a balanced description of both the neutral Rydberg states converging to the ground state of the ion, as well as the electronic resonant states that cross the ionic potential. These electronic resonance states are neutral Rydberg states with an excited ionic core. The PECs of ArH^+ and electronically excited states of ArH have previously been computed in Ref. [29] using the multireference averaged quadratic coupled cluster method.

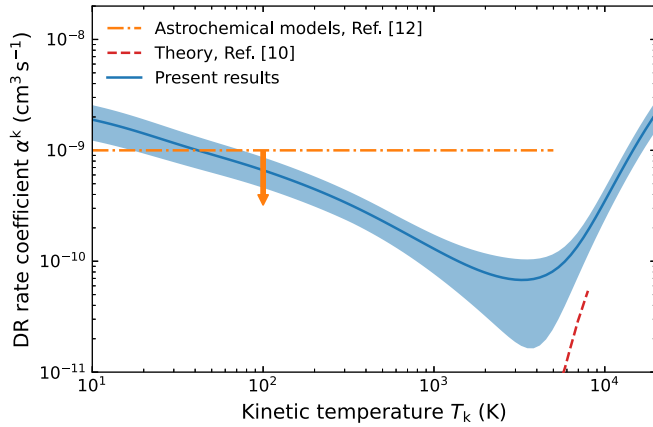


FIG. 6. Comparison of the kinetic-temperature-dependent DR rate coefficient α^k from our present experiment to previously published data. Here, the downward pointing arrow indicates that the value of $1 \times 10^{-9} \text{ cm}^3 \text{ s}^{-1}$ was taken as an upper limit in Ref. [13]. The shaded area around the present results corresponds to the total systematic uncertainty of the measurement, mainly due to the absolute scaling of α^{mb} and the uncertainty of T_{\perp} . The particular contributions of these uncertainties have been discussed previously [18]. In the region of the lowest values, the statistical counting uncertainties were also taken into account, as described in the text.

In Fig. 7, the presently calculated adiabatic PECs of ArH in ${}^2\Sigma^+$ symmetry are displayed as thin blue curves. This symmetry is important for low-energy DR of ArH^+ . The thick red curve is the ground-state PEC of the ion. The energy scale is relative to the $v = 0$ vibrational level of the ArH^+ ion (denoted by the red dashed line). All PECs were calculated using the multireference configuration interaction (MRCI) method [30]. To describe both the Rydberg states below the ground state of the ion as well as the neutral resonance states, we used natural orbitals generated using MRCI calculations on the ionic ground state $X^1\Sigma^+$ as well as the first excited $A^1\Sigma^+$

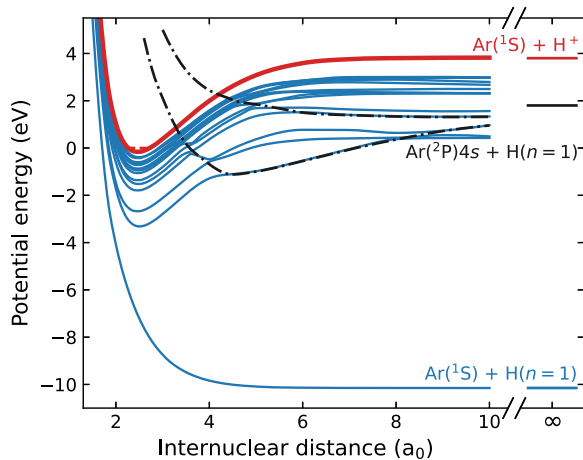


FIG. 7. Adiabatic PECs of ArH in ${}^2\Sigma^+$ symmetry (thin blue curves), as well as the PEC of the ground electronic state of ArH^+ (thick red curve) and its lowest vibrational level (dashed red line). The dotted-dashed black curves display the potentials of quasidiabatic resonant states that contribute to the direct DR. The horizontal full lines show the dissociation limits as given in Fig. 1.

state of the ion. The $1\sigma, 2\sigma, 3\sigma, 1\pi$ (composed primarily of $1s, 2s,$ and $2p$ Ar atomic orbitals) were kept doubly occupied, and the reference space of five natural orbitals, consisting of $4\sigma, 5\sigma, 2\pi,$ and 6σ , was used. The basis set was composed of $(12s, 5p, 2d)$ primitive basis functions contracted to $[6s, 5p, 2d]$ for argon, while $(11s, 6p, 4d, 1f)$ primitive functions contracted into $[8s, 6p, 4d, 1f]$ was used for hydrogen. Single and double external excitations were included when the natural orbitals were calculated. The natural orbitals were then further expanded with $(7s, 4p, 3d)$ basis functions centered on argon. The adiabatic PECs of ArH were computed using an MRCI in this expanded orbital space. Again, the lowest five orbitals were frozen. Full CI was carried out in the reference space of the five natural orbitals described above and, in addition, single external excitations out of the reference configurations were included. The calculations were carried out using the MESA program [31].

The dotted-dashed black curves in Fig. 7 display “quasidiabatic” PECs of the resonance states. These were abstracted from the structure calculations by analyzing the CI coefficients of the adiabatic wave functions. The resonant states are Rydberg states converging to electronically excited ionic cores. These cores have the 5σ orbital or 2π orbital singly excited. When the potentials of these states are above the ion potential, they should be computed using electron scattering calculations as was done in Refs. [10,11]. Here, we only want to illustrate the DR mechanism and use potentials extracted from structure calculations.

Note that the potentials of the resonant states cross the ion potential at internuclear distances much larger than the equilibrium distance of the ion. The resonance states correlate with asymptotic dissociation limits that are energetically closed at low collision energies. The same applies to electronic resonant states in ${}^2\Pi$ symmetry not displayed in the figure. At low energies, the only state that is open for dissociation is the electronic ground state. The electron is, therefore, initially captured into a rovibrationally excited Rydberg state which subsequently predissociates by nonadiabatic couplings to the ground state as observed here experimentally.

V. DISCUSSION

Our combined merged-beams rate coefficient and 3D imaging measurements at low collision energies ($E_d \lesssim 0.1 \text{ eV}$) confirmed the existence of a DR pathway for ArH^+ that results in ground-state atomic products. This pathway was not detected in previous room-temperature measurements, due to experimental limitations [7]. In the absence of resonance states that correlate with the ground-state atomic limit and cross the ionic PEC, we conclude that the low-energy DR of ArH^+ is driven by nonadiabatic interactions where dissociation occurs on the loosely bound PEC of electronic ground-state ArH.

Predissociation of bound Rydberg states for ArH has been previously observed in electronic spectra and investigated by theory for selected states (e.g., Refs. [32,33] and references therein). Calculations predict a complex dependence of the predissociation lifetime on the electronic, vibrational, and rotational states. They also highlight the sensitivity of the calculated predissociation lifetimes to the PECs. Additionally,

in low-energy DR of ArH^+ , a range of autoionizing intermediate ArH Rydberg states are involved. The complex interplay between autoionization and predissociation is expected to be reflected in the DR mechanism and in the resonant features observed in the DR cross section.

Our present merged-beams rate coefficient already contains hints at the underlying resonant features in the cross section. They are best highlighted in Fig. 3 when compared to the featureless E^{-1} cross-section model under the assumption of a constant DR probability that is independent of energy [3]. The measured data show statistically significant deviations at 25 and 75 meV in the form of dips, and at 15 meV in the form of a peak. Also between 0.1 and 1 eV, the experimental average value is significantly smaller than our E^{-1} cross-section model. The identification of the corresponding intermediate ArH Rydberg states at these collision energies is beyond the scope of this paper. Our results will be a stringent test for future theoretical cross-section calculations down to collision energies of a few meV. For theoretical models incorporating the rotational structure, a comparison can be made by using the experimental rotational-level populations, given in Appendix A.

For energies $\gtrsim 1$ eV, our measured $\alpha^{\text{mb}}(E_d)$ closely follows the theoretical results of Refs. [10,11]. Minor discrepancies can be seen near the threshold for the first excited Ar products at ≈ 2 eV, where our values systematically exceed the theoretical ones. This could result from a limitation of the cross-section conversion method, inaccuracies of the theoretical model close to threshold, or a contribution of the excited $\text{H}(n=2)$ DR products. The latter, even though not correlated with any of the theoretical ArH resonance states, are energetically accessible. We made a dedicated search using our 3D imaging technique between 2 to 3 eV for $\text{H}(n=2)$ products but found no statistically significant signal. For the present measurements we conclude that a 10 times or more greater sensitivity would be required to gain further insights into this matter.

There is an evident discrepancy at low energies between our present results and the theory of Refs. [10,11]. This can be explained by the absence of the ground state for ArH as a potential dissociation pathway in the published theoretical model. This state will need to be included in any future model trying to reproduce our present results. The discrepancy at low energies also leads to a considerable difference for $\alpha^k(T_k)$. The missing cross section contributes even at a few thousand K and the theoretical results fall outside the lower error band of our measurements.

To describe the process theoretically, MQDT calculations are currently being performed; these will be reported in a future study. Compared with the other rare gas diatomic hydrides HeH^+ and NeH^+ , the theoretical description of DR of ArH^+ is more challenging. This is not only because there are more electrons in the system, but also because it is crucial to have a balanced description of both the Rydberg states and the doubly excited resonant states. The HeH and NeH systems have no doubly excited states interacting with the Rydberg manifolds situated below the ground state of the ions. Preliminary calculations show that the mixing of orbital angular momentum of the scattered electron, manifesting as off-diagonal elements in the quantum defect matrix $\mu_{ll'}(\epsilon, R)$,

is essential to include in the theoretical model. Here, l and l' are the orbital angular momenta of the incoming and scattered electrons, respectively, ϵ is the scattering energy, and R is the internuclear distance of the target ion. These matrix elements can be extracted from fixed nuclei electron scattering calculations as was done, e.g., in Ref. [8], where the quantum defect matrix was obtained from the background phase shifts of the scattering matrix. The electron scattering calculations have to be performed with origin at the center of charge of the molecular ion [8]. We have found that compared to the resonant part of the scattering matrix that describes the contribution from the scattering resonant states, the background phase shifts are much more sensitive to the accuracy of the electron scattering calculation performed. We will return to this matter in our future study.

For astrochemical applications, it is important to note that our $\alpha^k(T_k)$ is determined for the experimental rotational population, corresponding to a rotational temperature of ≈ 20 K. Rotational-level-specific results were beyond the possibilities of the measurements, however, for low temperatures $T_k \lesssim 1000$ K, we can derive an extreme upper limit for the $J=0$ level. By assuming that only the $J=0$ level is responsible for the observed data, the upper limit equals the experimental $\alpha^k(T_k)$ divided by the $J=0$ population. For high temperatures, this limit is not recommended since we do not expect a significant rotational-level dependence for the underlying cross section.

VI. SUMMARY

Here, we have reported the first quantitative DR measurement for ArH^+ in its lowest rotational levels and at collision energies $\lesssim 1$ eV. We have measured its merged-beams rate coefficient over a wide energy range and on an absolute scale. The measurements were further augmented by 3D imaging to determine the internal state of the DR products and gain insight into the recombination pathways. By combining the results, we have demonstrated that the low-energy DR of ArH^+ is driven by nonadiabatic interactions and its main dissociation pathway is the electronic ground state of ArH.

In the absence of *ab initio* calculations for the low-energy DR pathway, we have compared our result to a featureless E^{-1} cross section. This comparison has demonstrated that the underlying cross section consists of resonant features. Within the framework of the indirect DR mechanism, the features are related to the Rydberg states of ArH. Our results can be directly used to benchmark theoretical models at a higher level of electronic complexity than what is typically considered in the literature. We have also compared our results to theoretical calculations for collision energies $\gtrsim 1$ eV where we have found satisfactory agreement.

Finally, we have derived a kinetic rate coefficient for use in chemical models from our results. For diffuse clouds and similar environments with low internal excitation, we have determined a stringent upper limit for the $J=0$ state-specific rate coefficient. In denser and hotter environments, like the Crab Nebula, our results represent a reliable constraint on the DR rate coefficient. In Table II, we have provided an analytical representation for our data.

TABLE II. Fit parameters for the ArH^+ kinetic temperature rate coefficient α^k and its lower and upper error bands from Fig. 6, using Eq. (D1).

Parameter	Rate coefficient	Lower error limit	Upper error limit
A	4.57×10^{-10}	3.21×10^{-10}	5.78×10^{-10}
n	0.295	0.314	0.311
c_1	6.38×10^{-8}	2.95×10^{-8}	8.93×10^{-8}
c_2	-1.93×10^{-6}	-1.32×10^{-6}	-2.62×10^{-6}
c_3	-1.04×10^{-5}	-8.63×10^{-6}	-1.41×10^{-5}
c_4	-3.05×10^{-5}	-2.77×10^{-5}	-3.12×10^{-5}
c_5	-7.50×10^{-5}	-9.20×10^{-5}	-7.76×10^{-5}
c_6	1.11×10^{-2}	1.06×10^{-2}	1.80×10^{-2}
c_7	1.71×10^{-1}	1.73×10^{-1}	2.39×10^{-1}
c_8	8.83×10^{-1}	7.20×10^{-1}	1.16×10^0
T_1	11.4	11.7	11.6
T_2	428	421	455
T_3	1180	1250	1270
T_4	2930	3140	3050
T_5	7170	8180	7440
T_6	41200	41700	42900
T_7	77200	84600	79400
T_8	139000	154000	142000

ACKNOWLEDGMENTS

Financial support by the Max Planck Society is acknowledged. A.K., D.A.N., D.P., D.W.S., and M.G.W. were supported in part by the NASA Astrophysics Research and Analysis program under Grant No. 80NSSC19K0969. L.W.I. and S.S. acknowledge financial support by the Deutsche Forschungsgemeinschaft (DFG, Grant No. 431145392). We thank J. Forer for fruitful discussions.

APPENDIX A: ROTATIONAL-LEVEL POPULATION EVOLUTION MODEL

In order to predict the rotational populations for the stored ArH^+ ions, we have adopted the collisional-radiative model and methodology developed for our previous studies of CH^+ and OH^+ ions [23,26]. Good agreement was found for CH^+ between the modeled and measured rotational populations.

The ArH^+ from our ion source are electronically, vibrationally, and rotationally excited. The lowest excited electronic states of ArH^+ are of repulsive character and the states above those are predissociating [34]. Thus, we expect all the ions to be in the $X^1\Sigma^+$ ground electronic state soon after injection. Calculations for vibrational transition probabilities within the ground electronic state find radiative lifetimes of < 6 ms [7]. Given the timescale of our experiments, on the order of several tens to hundreds of seconds, we can safely assume that the ions for our measurements were in their ground electronic and vibrational states.

The rotational energies of $\text{ArH}^+ X^1\Sigma^+(v=0)$ were calculated using the B_0 and D_0 spectroscopic constants of Ref. [35] as

$$E_J = B_0[J(J+1)] - D_0[J(J+1)]^2. \quad (\text{A1})$$

Levels up to $J = 49$ were included in the model. We used the theoretical 2.177 D dipole moment of Ref. [36] to calculate

Einstein coefficients for spontaneous emission for rotational transitions using Eq. (S1) from Ref. [23].

The ambient radiation field in CSR is accounted for by adopting the two-component model of Ref. [22]. It is the sum of the thermal radiation of the cryogenic chambers and the room-temperature leaks from various openings in CSR. Here, the cryogenic component is estimated to be $T_{\text{low}} \approx 6$ K, based on the measured chamber temperatures. The room-temperature component is fixed to 300 K. Previous work has found its fraction relative to the total photon occupation number to be $\varepsilon = (1.0 \pm 0.3) \times 10^{-2}$ [23].

Rotational-level-changing collisions between electrons and ions are also present in our experimental setup [23]. To include the effects of these collisions, we used the theoretical electron-impact rotational excitation cross sections from Ref. [37] for $\Delta J = 1$ and 2 transitions of ArH^+ . The corresponding deexcitation cross sections were obtained by applying the principle of detailed balance. Rotational-level-changing merged-beams rate coefficients were then calculated for all E_d corresponding to those used for our DR rate coefficient measurements. For a given transition, the importance of rotational-level-changing collisions can be shown by the ratio of the Einstein $A_{J' \rightarrow J''}$ rate ($J' > J''$) to the J -level-changing merged-beams rate coefficient $\alpha_{J' \rightarrow J''}$. This gives the critical electron density

$$n_c = A_{J' \rightarrow J''} / \alpha_{J' \rightarrow J''}. \quad (\text{A2})$$

Our DR measurements here were carried out for ions primarily in the $J \leq 1$ levels. For the $J' = 1 \rightarrow J'' = 0$ transition, we calculated $A_{1 \rightarrow 0} = 4.3 \times 10^{-3} \text{ s}^{-1}$ and a critical electron density of $(0.9 \pm 0.2) \times 10^3 \text{ cm}^{-3}$ at matched velocities. This critical density is an order of magnitude smaller than the typical ring-averaged electron density of $(9.4 \pm 0.9) \times 10^3 \text{ cm}^{-3}$ for our measurements, meaning that collisions dominate the rotational-level-changing rates in our experiment for the $J \leq 1$ levels.

The DR measurement scheme consisted of two ion storage phases. In the first phase, following injection, we applied electron cooling at matched velocities for 42 s. For the second phase, we measured for predefined sets of E_d for 408 s. The α^{mb} data shown in Fig. 3 have been evaluated for storage times > 42 s, where the rotational-level populations were within 20% of their final values.

The corresponding modeled relative populations are shown in Fig. 8 for the levels of interest ($J \leq 2$) as a function of storage time from injection. The initial rotational-level populations are given by a Boltzmann distribution within the ground vibrational state. The final population results for levels $J \leq 2$ are insensitive to the initial populations for initial rotational temperatures of > 300 K.

The main model uncertainties are due to the experimental parameters T_{\perp} , T_{low} , and ε . The dipole moment and the electron-impact rotational excitation cross sections for ArH^+ can also affect the model predictions. However, the magnitudes of these last two parameters primarily affect the timescale of the rotational population evolution. For the present results, when the populations are close to equilibrium, the uncertainties of these last two parameters do not significantly impact the accuracy of our predictions.

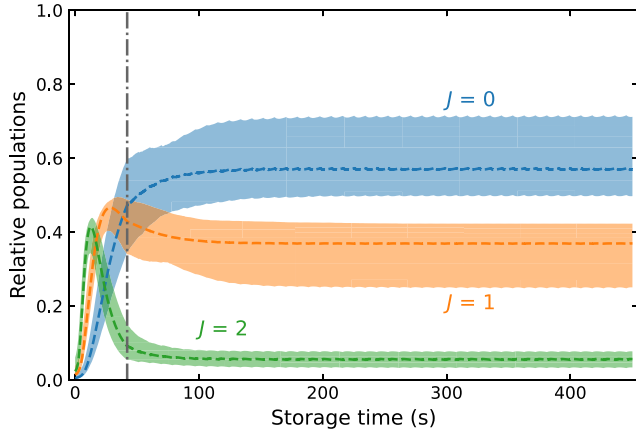


FIG. 8. Collisional-radiative model of ArH^+ rotational-level population evolution as a function of ion-storage time for our DR measurements. The dashed lines are for the mean model with the parameters $k_B T_\perp = 2$ meV, $T_{\text{low}} = 6$ K, $\varepsilon = 1.0 \times 10^{-2}$, and a 3000-K initial rotational temperature. The accompanying shaded areas indicate the uncertainty of the predictions when varying these parameters, the dipole moment, the electron-impact rotational excitation cross sections, and the initial rotational temperature, all within their estimated uncertainties (see text). The vertical dotted-dashed line marks the beginning of the DR data acquisition period.

The model uncertainty determination uses the Monte Carlo approach of Ref. [26]. The dipole moment, electron impact rotational excitation cross sections, and ε were drawn from normal distributions. For the dipole moment, we estimated an uncertainty of 10%, based on the scatter of theoretical results (e.g., Refs. [34,36] and references therein). For the cross sections, the systematic uncertainty at all energies and for all levels was assumed to be 40%, based on our CH^+ measurements [23]. The initial rotational temperature, T_{low} , and T_\perp were drawn from uniform distributions to include the physical limits on these parameters. For the initial rotational temperature, a lower limit of 300 K and an upper limit of 5000 K were chosen. For T_{low} , the lower and upper limits were set to 4 and 8 K, respectively, which have an insignificant impact on the results. For $k_B T_\perp$, we used the previously determined range from 1 to 3 meV. At each storage time, the uncertainties were evaluated as the 16th and 84th percentiles of the population distributions, which is equivalent to \pm one-sigma for a normal distribution. The shaded areas in Fig. 8 are given for these percentiles.

Using our model, we estimate the average relative populations of the rotational levels in the measurement time window to be $0.57^{+0.13}_{-0.08}$ for $J = 0$, $0.37^{+0.06}_{-0.11}$ for $J = 1$, and $0.06^{+0.02}_{-0.03}$ for $J = 2$. The uncertainties for the two lowest J levels are anticorrelated and the sum of their populations totals to ≈ 0.94 .

APPENDIX B: 3D IMAGING ANALYSIS

Imaging the dissociation fragments in our DR measurements enables us to determine the kinetic energy released, E_{KER} , in the DR process. We use this to identify the internal state of the fragments after dissociation. Unambiguous determination of E_{KER} is achieved by combining the measured distance between the fragments in the detector plane d_\perp

(assumed to be perpendicular to the ion beam direction) and the difference in the arrival time Δt of the fragments. This method is referred to as 3D imaging (e.g., Ref. [38]). From Δt we determine the distance between the fragments parallel to the beam direction as

$$d_\parallel = v_{\text{ion}} \Delta t, \quad (\text{B1})$$

where v_{ion} is the ion beam velocity in the laboratory frame. From the combination of d_\perp and d_\parallel we can determine the distance between the fragments along the axis of dissociation. This is proportional to the velocity

$$v_{\text{KER}} = \sqrt{\frac{2E_{\text{KER}}}{M}}, \quad (\text{B2})$$

where $M = m_A + m_B$ is the total mass of the heavier m_A and lighter m_B fragments.

In our measurements, the velocities of the fragments differ significantly from v_{ion} so that we cannot use the approximations of Ref. [38] to accurately determine E_{KER} . Here, we included the necessary corrections to the 3D imaging analysis, expanded in the velocity ratio $r_v = v_{\text{KER}}/v_{\text{ion}}$. It was sufficient to implement these corrections to first order in r_v . For a detailed derivation of the corresponding equations, see Ref. [27].

The relationship between E_{KER} and the measured distances d_\perp and d_\parallel , taking these corrections into account, is given by

$$\begin{aligned} \sqrt{E_{\text{KER}}} &= \sqrt{E_{\text{ion}}} \frac{m_A + m_B}{\sqrt{m_A m_B}} \frac{m_A m_B}{|C(s)|} \\ &\times \sqrt{1 + \left(\frac{d_\perp}{d_\parallel} \frac{C(s)}{C(s) - 2m_A m_B} \right)^2}, \end{aligned} \quad (\text{B3})$$

where

$$C(s) = \frac{s}{d_\parallel} (m_A + m_B)^2 + m_A^2 - m_B^2, \quad (\text{B4})$$

and s is the distance between the dissociation point and the detector. In order to apply this correction, the masses of the fragments have to be determined, which is reflected in the sign of d_\parallel . We define $d_\parallel > 0$ when the heavier fragment m_A arrives first at the detector and negative when m_B arrives first.

The mass assignment of the imaging data is done in four steps. First, we estimate the average ion beam center projected from the interaction region onto the detector. Second, we assign masses to the impact positions within individual events based on their distance to the projected beam center in the detector plane. Third, we determine center-of-mass positions in the detector plane for all the detected dissociation events and recalculate the projected ion beam center. We repeat the second and third steps until convergence for the projected beam center is achieved. Fourth, to determine which particle arrived first, we make use of the positive correlation between the amplitude of the electrical signals of the MCP (arrival times) and the brightness of phosphor screen spots (impact positions) [39]. The signal amplitudes are not clearly correlated with particle mass, but rather establish a connection between the two detection systems. Additional details about the procedure can be found in Ref. [27].

The measured imaging data represent the sum of both DR events and background from residual-gas-induced collisions. The DR events originate within the well-defined overlap

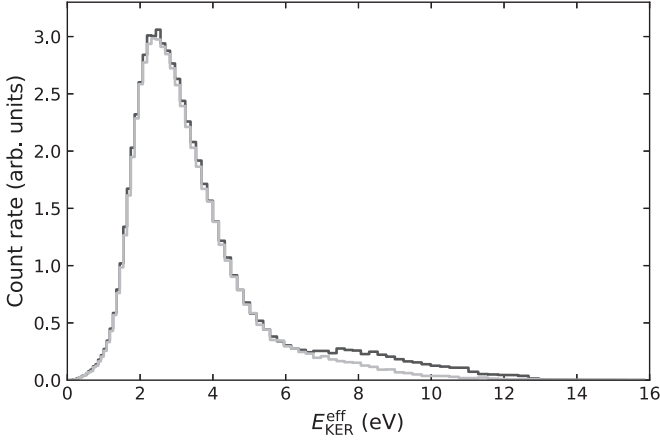


FIG. 9. Measured $E_{\text{KER}}^{\text{eff}}$ distributions in the electrons-off step (gray) and in the measurements step (black) at matched velocities ($E_d = 0$ eV). The data measured in the electrons-off step are due to residual-gas-induced events. For $E_{\text{KER}}^{\text{eff}} \lesssim 7$ eV, the electrons-off data overlap with the data recorded in the measurements step. Above ≈ 7 eV, the difference signal corresponds to DR of ArH^+ .

region between the electron and ion beams. The mean distance from the overlap region to the particle detector is $L_0 = 3807$ mm. Since we cannot individually determine where each event originates from, we evaluate Eq. (B3) by approximating $s \approx L_0$, leading to a distribution of effective $E_{\text{KER}}^{\text{eff}}$, as shown in Fig. 9. The background contribution is measured using the $E_{\text{KER}}^{\text{eff}}$ histogram for the electrons-off step. This background is subtracted from the measured $E_{\text{KER}}^{\text{eff}}$ histogram for the measurement step at E_d . The difference produces the electron-induced signal shown, e.g., in Fig. 4.

The $E_{\text{KER}}^{\text{eff}}$ histogram for DR events for a single DR channel with a given E_{KER} , such as Fig. 4, can be modeled empirically by the combination of a uniform distribution that takes into account the central part of the overlap region where the collision energies are close to E_d and a Gaussian smoothing that represents the transition into and out of this central region. The uniform distribution is parametrized by the length ΔL of the overlap region. The Gaussian distribution is parametrized by the smoothing parameter δ . This is to account for how in the transition into and out of the central region, the DR signal typically drops rapidly due to the decrease of the DR cross section with increasing collision energy. The resulting weighted probability density function is given as

$$\begin{aligned}
 P(\sqrt{E_{\text{KER}}^{\text{eff}}}) &= \frac{IL_0}{2\Delta L\sqrt{E_{\text{KER}}}} \\
 &\times \left[\text{erf}\left(\frac{\sqrt{E_{\text{KER}}^{\text{eff}}} - \sqrt{E_{\text{KER}}} + \sqrt{E_{\text{KER}}}\Delta L/(2L_0)}{\sqrt{2}\delta}\right) \right. \\
 &\left. - \text{erf}\left(\frac{\sqrt{E_{\text{KER}}^{\text{eff}}} - \sqrt{E_{\text{KER}}} - \sqrt{E_{\text{KER}}}\Delta L/(2L_0)}{\sqrt{2}\delta}\right) \right], \tag{B5}
 \end{aligned}$$

where I is a weighting factor so that the integral of the distribution function is equal to that of the measured histogram.

Due to the large mass difference between Ar and H, the dissociation of ArH^+ can result in d_{\perp} larger than the imaging detector radius of 60 mm, starting at $E_{\text{KER}} \approx 1.5$ eV. Since d_{\perp} is also a function of dissociation location and distance s , the finite size of the detector introduces a complex geometrical cutoff on the measured $E_{\text{KER}}^{\text{eff}}$ histogram. To be able to use the empirical model given by Eq. (B5), we select a subset of the imaging data that is unaffected by the finite detector size. As the selection criterion, we evaluate the polar angle ϑ between the beam direction and the internuclear axis. This angle is defined as

$$\vartheta = \begin{cases} \arctan\left(\frac{d_{\perp}}{d_{\parallel}} \frac{C(s)}{C(s)-2m_{\Lambda}m_{\text{B}}}\right), & d_{\parallel} > 0 \\ \pi + \arctan\left(\frac{d_{\perp}}{d_{\parallel}} \frac{C(s)}{C(s)-2m_{\Lambda}m_{\text{B}}}\right), & \text{otherwise} \end{cases} \tag{B6}$$

with $s \approx L_0$. By using ϑ as the selection criterion, we detect events independent of their origin s . In particular, we applied this selection criterion to the data plotted in Fig. 4.

The detector setup used in the present measurements has additionally limitations for ArH^+ dissociation events with $E_{\text{KER}} \lesssim 1$ eV. The electronic system is not able to distinguish particle hits with time differences $\Delta t \lesssim 10$ ns. In particular, for $E_{\text{KER}} \lesssim 0.1$ eV, no 3D imaging data can be collected. The limitations of the electronic readout and detector size translate into a 3D-imaging efficiency as a function of E_{KER} . It reaches its maximum when d_{\perp} is close to the detector size, for ArH^+ at $E_{\text{KER}} \approx 1.5$ eV. Above this energy, the efficiency gradually decreases as E_{KER} increases. As a result, the data shown in Fig. 5 only provide a qualitative insight into the branching ratios of possible DR channels.

APPENDIX C: BEAM PURITY ANALYSIS

The purity of the stored ArH^+ ion beam was essential in order to confidently interpret the observed low-energy electron-induced count rate as being due to DR of ArH^+ . The DR rate coefficient α^{mb} of ArH^+ was expected to be on the order of $1 \times 10^{-9} \text{ cm}^3 \text{ s}^{-1}$ or lower. Any other ions with a fractional contamination of $\gtrsim 1 \times 10^{-3}$ and an $\alpha^{\text{mb}} \gtrsim 1 \times 10^{-6} \text{ cm}^3 \text{ s}^{-1}$, typical for DR of most molecular ions, would produce a comparable or larger electron-induced signal. However, such a large DR rate coefficient, combined with the ion storage time, also results in the efficient destruction of the contaminants compared to ArH^+ in our study.

The initial purity of the stored ArH^+ ion beam was established prior to the DR measurements. The ions extracted from the ECR ion source underwent mass selection through a series of dipole magnets prior to injection into CSR. These were sufficient to separate species differing by ~ 1 u from ArH^+ . The stored ion beam was further mass analyzed by operating CSR in the so-called isochronous mode, i.e., as a time-of-flight mass spectrometer with a mass resolution of $\sim 10^{-5}$ u [24]. The analysis confirmed the presence of C_3H_5^+ corresponding to $\sim 1 \times 10^{-3}$ of the total injected ion number and an even smaller fraction of CH_3CN^+ .

As a followup on the ion beam composition, we investigated the electrons-on signal at matched velocities as a

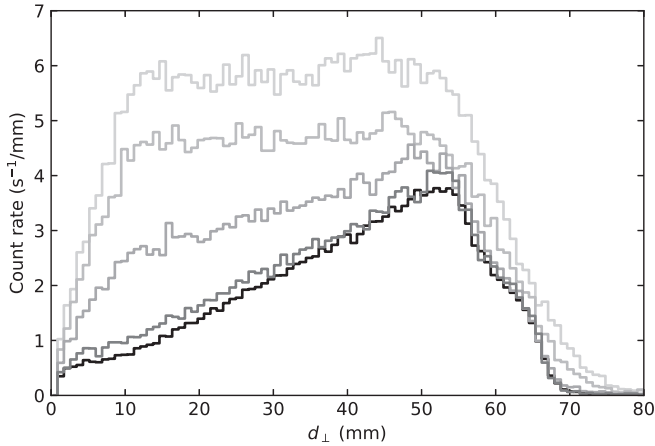


FIG. 10. Storage-time-dependent d_{\perp} distributions for electrons on at matched electron-ion velocities. The selected histograms ranging from light to dark gray are for storage times 0 to 5, 5 to 10, 15 to 20, 30 to 35, and 50 to 100 s, respectively. The darkest gray histogram is representative for the signal due to breakup of ArH^+ , present at all storage times. The data at earlier storage times are the sum of the ArH^+ and any contaminant ion signal.

function of storage time from injection up to 200 s. During the first 42 s, the electron beam was tuned to matched velocities and kept on at all times. The electrons-on signal contained contributions from DR, residual-gas-induced collisions, and the detector dark rate, as explained in Sec. II B. Both the count rate and imaging data revealed a strong time-dependent component in the measured electrons-on signal that we associate with the selective depletion of ion beam contaminants that have large DR rate coefficients.

The imaging data were used to verify that the time-dependent component of the electrons-on signal does not originate from DR of ArH^+ . We analyzed events that resulted in the detection of two particles. Representative histograms of d_{\perp} for several storage time windows are shown in Fig. 10. The plotted histograms show a decay of the measured count rate in each bin toward the shape characteristic for all storage times above ≈ 50 s. This part, present at all storage times, has been identified as the breakup of ArH^+ due to DR and residual-gas-induced collisions. As indicated by 3D imaging, the breakup of ArH^+ can lead up to $d_{\perp} \approx 150$ mm, however, the finite size of the imaging detector introduces a complex cutoff for $d_{\perp} > 50$ mm. The additional signal at storage times < 50 s, which we attribute to DR of contaminant ions, is most pronounced at smaller values of d_{\perp} . Residual-gas-induced collisions for contaminant ions are assumed to be negligible, as discussed below. For ArH^+ to produce the observed imaging signal at small d_{\perp} , several breakup channels with E_{KER} ranging from 0.1 to 1 eV would need to be involved. This would imply electronically or vibrationally excited states with $E(\text{ArH}^+) > 0.5$ eV that decay on timescales of several seconds. According to our collisional-radiative model, there are no such states existing for ArH^+ , thereby ruling out this scenario.

The storage-time-dependent count rate data further enabled us to estimate α^{mb} at matched velocities for the contaminant ions. To be able to separate the DR signal at all storage times,

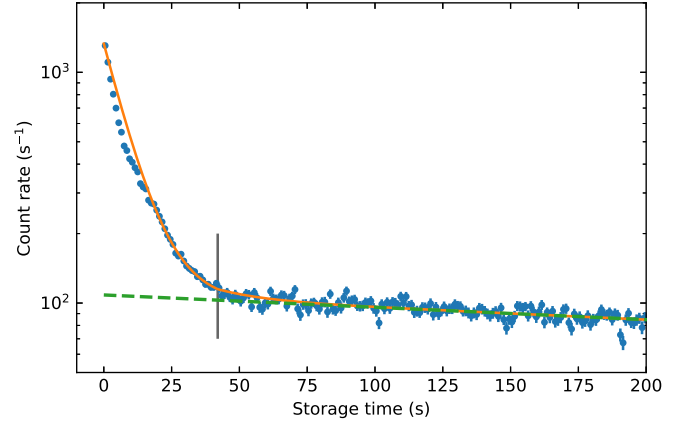


FIG. 11. Electron-induced count rate as a function of storage time. The measured data are plotted as the symbols with one-sigma statistical error bars. The effective two-component model described in the text is plotted as the orange full line. The model was fitted to the data from 17 to 200 s and extrapolated to earlier storage times. The ArH^+ component is plotted as the green dashed line. The gray vertical line highlights 42 s.

we needed to estimate the non-electron-induced contributions that were monitored only for storage times > 42 s in the electrons-off step of our measurement scheme. To account for ion losses, we modeled the storage time dependence of the residual-gas-induced count rate with a single-term exponential function from 42 to 200 s and extrapolated it to earlier storage times. This approach assumes that the residual-gas-induced count rate is proportional to the number of stored ions and that it is dominated by ArH^+ . Even if residual-gas-induced collisions were an order of magnitude more efficient for the contaminant ions, the extrapolation is well justified by the small fraction ($\sim 1 \times 10^{-3}$) of contaminant ions injected into the storage ring. The extracted electron-induced count rate due to DR of ArH^+ and contaminant ions as a function of storage time is shown in Fig. 11.

To quantify the observed storage-time dependence of the electron-induced signal we constructed a model, consisting of the sum of two single-term exponential functions. The slow decaying part represented ArH^+ with the same ion loss rate as determined from the residual-gas-induced count rate. The fast decaying part represented the contaminant ions with a fitted DR depletion rate. Additional loss processes for the contaminant ions, e.g., due to ion storage effects, are expected to contribute on the same order of magnitude as observed for ArH^+ and are negligible in our analysis. The DR depletion rate of a given species is given by the species-specific α^{mb} multiplied with the ring-averaged electron density. In the model, we also took into account the change in effective electron density when additional electrons-off steps were present in the measurement after 42 s of ion storage. The free parameters of the model were determined from a least-squares fit to the measured data for storage times from 17 to 200 s, i.e., where the simple model best represents the data. At earlier storage times, the model only qualitatively reproduces the data. This is most likely due to a combinations of the following effects. After injection, the ion beam underwent phase-space cooling that increased the overlap between the

ion and electron beams, leading to a change in the effective electron density. Additionally, both ArH^+ and contaminant ions are expected to undergo internal cooling that could both increase or decrease their respective α^{mb} as a function of storage time. A possibly larger ion loss rate after injection due to ion storage effects when compared to that of a phase-space cooled beam would be underestimated by the extrapolation method.

From our model, we have determined a fitted depletion rate for the contaminant ions to estimate $\alpha^{\text{mb}} \approx 1 \times 10^{-5} \text{ cm}^3 \text{ s}^{-1}$. This value multiplied by the independently determined fraction of contaminant ions at injection ($\sim 1 \times 10^{-3}$) indicates an order of magnitude larger electron-induced count rate for the contaminant ions compared with that for ArH^+ , in agreement with the observed count rate data at the earliest storage times. To summarize, the magnitude and the storage time dependence of the fast decaying electron-induced signal relative to ArH^+ indicate the presence of contaminant ions that undergo DR with $\alpha^{\text{mb}} \approx 1 \times 10^{-5} \text{ cm}^3 \text{ s}^{-1}$ at matched velocities. As a result of this high DR rate coefficient, the stored contaminant ions were rapidly depleted from the ion beam, thereby producing an essentially pure stored ArH^+ ion beam.

APPENDIX D: KINETIC TEMPERATURE DR RATE COEFFICIENT

Here, we provide an analytic representation for the ArH^+ DR kinetic temperature rate coefficient α^{k} and its one-sigma error band shown in Fig. 6. We follow Ref. [25] and fit α^{k} with a function optimized to account for typical DR features, i.e., broad peaks or dips from resonances. The fit function is given by

$$\alpha^{\text{k}}(T_{\text{k}})[\text{cm}^3 \text{ s}^{-1}] = A \left(\frac{300}{T_{\text{k}}[\text{K}]} \right)^n + T_{\text{k}}[\text{K}]^{-1.5} \sum_{r=1}^N c_r \exp\left(-\frac{T_r}{T_{\text{k}}[\text{K}]}\right), \quad (\text{D1})$$

and the parameters are listed in Table II. The maximum relative deviation of the fit is 0.3%.

TABLE III. Fit parameters for the ArH^+ kinetic temperature rate coefficient α^{k} and its relative uncertainty from Fig. 6, using Eqs (D2) and (D3), respectively.

Parameter	Temperature range (K)			
	10–100	100–1500	1500–7000	7000–20 000
A	3.82×10^{-10}	3.89×10^{-10}	2.47×10^{-13}	5.06×10^{-13}
β	−0.503	−0.861	1.758	2.084
γ	1.027	42.2	−4680	7540
F_0	1.32	1.44	0.594	1 440 000
g	1.042	−11.9	−344	4260

We also give the Arrhenius-Kooij (AK) representation, as is typically used in astrochemistry, combustion chemistry, and other chemical models and databases. Following the approach of Ref. [18], we provide a set of piecewise-joined fit functions on several temperature intervals since we cannot model the experimental results with a single AK fit function. This approach introduces discontinuities in the temperature dependence of the analytical rate coefficient between the temperature intervals, which can be avoided by using the representation by Eq. (D1). The temperature-interval fit function is given by

$$\alpha^{\text{k}}(T_{\text{k}})[\text{cm}^3 \text{ s}^{-1}] = A \left(\frac{T_{\text{k}}[\text{K}]}{300} \right)^{\beta} e^{-\frac{\gamma}{T_{\text{k}}[\text{K}]}}. \quad (\text{D2})$$

The parameters for each temperature interval are listed in Table III. The maximum relative deviation of the fit is 10.8%. Following the conventions of Ref. [40], the relative uncertainty is described by the log-normal factor $F = \exp(\Delta\alpha^{\text{k}}/\alpha^{\text{k}})$. This quantity is fitted on the same temperature intervals as for the AK fits by the fit function

$$F(T_{\text{k}}) = F_0 \exp\left[g\left(\frac{1}{T_{\text{k}}[\text{K}]} - \frac{1}{300}\right)\right]. \quad (\text{D3})$$

Due to the asymmetric error bands of α^{k} , the log-normal factor is calculated as the average of the upper and lower error bands. The continuity of both the α^{k} and error fits are guaranteed on the border of each temperature range.

- [1] W. D. Geppert and M. Larsson, Dissociative recombination in the interstellar medium and planetary ionospheres, *Mol. Phys.* **106**, 2199 (2008).
- [2] A. I. Florescu-Mitchell and J. B. A. Mitchell, Dissociative recombination, *Phys. Rep.* **430**, 277 (2006).
- [3] M. Larsson and A. E. Orel, *Dissociative Recombination of Molecular Ions* (Cambridge University Press, Cambridge, 2008).
- [4] J. Forer, D. Hvizdoš, X. Jiang, M. Ayouz, C. H. Greene, and V. Kokoouline, Unified treatment of resonant and nonresonant mechanisms in dissociative recombination: Benchmark study of CH^+ , *Phys. Rev. A* **107**, 042801 (2023).
- [5] S. L. Guberman, Dissociative recombination without a curve crossing, *Phys. Rev. A* **49**, R4277(R) (1994).
- [6] J. B. A. Mitchell, O. Novotny, G. Angelova, J. L. LeGarrec, C. Rebrion-Rowe, A. Svendsen, L. H. Andersen, A. I. Florescu-Mitchell, and A. E. Orel, Dissociative recombination of rare gas hydride ions: I. NeH^+ , *J. Phys. B: At. Mol. Opt. Phys.* **38**, 693 (2005).
- [7] J. B. A. Mitchell, O. Novotny, J. L. LeGarrec, A. Florescu-Mitchell, C. Rebrion-Rowe, A. V. Stolyarov, M. S. Child, A. Svendsen, M. A. El Ghazaly, and L. H. Andersen, Dissociative recombination of rare gas hydride ions: II. ArH^+ , *J. Phys. B: At. Mol. Opt. Phys.* **38**, L175 (2005).
- [8] Roman Čurík, D. Hvizdoš, and C. H. Greene, Dissociative recombination of cold HeH^+ ions, *Phys. Rev. Lett.* **124**, 043401 (2020).
- [9] O. Novotný, P. Wilhelm, D. Paul, A. Kálosi, S. Saurabh, A. Becker, K. Blaum, S. George, J. Göck, M. Grieser, F. Grussler, R. von Hahn, C. Krantz, H. Kreckel, C. Meyer, P. M. Mishra, D. Muell, F. Nuesslein, D. A. Orlov, M. Rimpler *et al.*, Quantum-state-selective electron recombination studies

- suggest enhanced abundance of primordial HeH⁺, *Science* **365**, 676 (2019).
- [10] A. Abdoulanziz, F. Colboc, D. A. Little, Y. Moulane, J. Z. Mezei, E. Roueff, J. Tennyson, I. F. Schneider, and V. Laporta, Theoretical study of ArH⁺ dissociative recombination and electron-impact vibrational excitation, *Mon. Not. R. Astron. Soc.* **479**, 2415 (2018).
- [11] E. Djuissi, A. Bultel, J. Tennyson, I. F. Schneider, and V. Laporta, Electron collisions with ArH⁺ molecular ions: highly excited vibrational states and dissociative excitation, *Plasma Sources Sci. Technol.* **31**, 114012 (2022).
- [12] M. J. Barlow, B. M. Swinyard, P. J. Owen, J. Cernicharo, H. L. Gomez, R. J. Ivison, O. Krause, T. L. Lim, M. Matsuura, S. Müller, G. Olofsson, and E. T. Polehampton, Detection of a noble gas molecular ion, ³⁶ArH⁺, in the crab nebula, *Science* **342**, 1343 (2013).
- [13] P. Schilke, D. A. Neufeld, H. S. P. Müller, C. Comito, E. A. Bergin, D. C. Lis, M. Gerin, J. H. Black, M. Wolfire, N. Indriolo, J. C. Pearson, K. M. Menten, B. Winkel, A. Sánchez-Monge, T. Möller, B. Godard, and E. Falgarone, Ubiquitous argonium (ArH⁺) in the diffuse interstellar medium: A molecular tracer of almost purely atomic gas, *Astron. Astrophys.* **566**, A29 (2014).
- [14] A. M. Jacob, K. M. Menten, F. Wyrowski, B. Winkel, and D. A. Neufeld, Extending the view of ArH⁺ chemistry in diffuse clouds, *Astron. Astrophys.* **643**, A91 (2020).
- [15] D. A. Neufeld and M. G. Wolfire, The chemistry of interstellar argonium and other probes of the molecular fraction in diffuse clouds, *Astrophys. J.* **826**, 183 (2016).
- [16] F. D. Priestley, M. J. Barlow, and S. Viti, Modelling the ArH⁺ emission from the crab nebula, *Mon. Not. R. Astron. Soc.* **472**, 4444 (2017).
- [17] R. von Hahn, A. Becker, F. Berg, K. Blaum, C. Breitenfeldt, H. Fadil, F. Fellenberger, M. Froese, S. George, J. Göck, M. Grieser, F. Grussie, E. A. Guerin, O. Heber, P. Herwig, J. Kartheim, C. Krantz, H. Kreckel, M. Lange, F. Laux *et al.*, The cryogenic storage ring CSR, *Rev. Sci. Instrum.* **87**, 063115 (2016).
- [18] D. Paul, M. Grieser, F. Grussie, R. von Hahn, L. W. Isberner, A. Kálosi, C. Krantz, H. Kreckel, D. Müll, D. A. Neufeld, D. W. Savin, S. Schippers, P. Wilhelm, A. Wolf, M. G. Wolfire, and O. Novotný, Experimental determination of the dissociative recombination rate coefficient for rotationally cold CH⁺ and its implications for diffuse cloud chemistry, *Astrophys. J.* **939**, 122 (2022).
- [19] N. Jain, A. Kálosi, F. Nuesslein, D. Paul, P. Wilhelm, S. G. Ard, M. Grieser, R. von Hahn, M. C. Heaven, E. Miliordos, D. Maffucci, N. S. Shuman, A. A. Viggiano, A. Wolf, and O. Novotný, Near-thermo-neutral electron recombination of titanium oxide ions, *J. Chem. Phys.* **158**, (2023).
- [20] H. Poth, Electron cooling: Theory, experiment, application, *Phys. Rep.* **196**, 135 (1990).
- [21] A. P. O'Connor, A. Becker, K. Blaum, C. Breitenfeldt, S. George, J. Göck, M. Grieser, F. Grussie, E. A. Guerin, R. von Hahn, U. Hechtischer, P. Herwig, J. Kartheim, C. Krantz, H. Kreckel, S. Lohmann, C. Meyer, P. M. Mishra, O. Novotný, R. Repnow *et al.*, Photodissociation of an internally cold beam of CH⁺ ions in a cryogenic storage ring, *Phys. Rev. Lett.* **116**, 113002 (2016).
- [22] C. Meyer, A. Becker, K. Blaum, C. Breitenfeldt, S. George, J. Göck, M. Grieser, F. Grussie, E. A. Guerin, R. von Hahn, P. Herwig, C. Krantz, H. Kreckel, J. Lion, S. Lohmann, P. M. Mishra, O. Novotný, A. P. O'Connor, R. Repnow, S. Saurabh *et al.*, Radiative rotational lifetimes and state-resolved relative detachment cross sections from photodetachment thermometry of molecular anions in a cryogenic storage ring, *Phys. Rev. Lett.* **119**, 023202 (2017).
- [23] A. Kálosi, M. Grieser, R. von Hahn, U. Hechtischer, C. Krantz, H. Kreckel, D. Müll, D. Paul, D. W. Savin, P. Wilhelm, A. Wolf, and O. Novotný, Laser probing of the rotational cooling of molecular ions by electron collisions, *Phys. Rev. Lett.* **128**, 183402 (2022).
- [24] M. Grieser, V. C. Schmidt, K. Blaum, F. Grussie, R. von Hahn, A. Kálosi, H. Kreckel, D. Müll, O. Novotný, F. Nuesslein, and A. Wolf, Isochronous mass spectrometry in an electrostatic storage ring, *Rev. Sci. Instrum.* **93**, 063302 (2022).
- [25] O. Novotný, A. Becker, H. Buhr, C. Domesle, W. Geppert, M. Grieser, C. Krantz, H. Kreckel, R. Repnow, D. Schwalm, K. Spruck, J. Stützel, B. Yang, A. Wolf, and D. W. Savin, Dissociative recombination measurements of HCl⁺ using an ion storage ring, *Astrophys. J.* **777**, 54 (2013).
- [26] A. Kálosi, L. Gamer, M. Grieser, R. von Hahn, L. W. Isberner, J. I. Jäger, H. Kreckel, D. A. Neufeld, D. Paul, D. W. Savin, S. Schippers, V. C. Schmidt, A. Wolf, M. G. Wolfire, and O. Novotný, Dissociative recombination of rotationally cold OH⁺ and its implications for the cosmic ray ionization rate in diffuse clouds, *Astrophys. J. Lett.* **955**, L26 (2023).
- [27] D. Paul, Electron recombination studies of rotationally cold CH⁺ ions at the cryogenic storage ring, Ph.D. thesis, Ruprecht-Karls-Universität Heidelberg, 2021.
- [28] See Supplemental Material at <http://link.aps.org/supplemental/10.1103/PhysRevA.110.022816> for tabulated experimental merged-beams rate coefficient.
- [29] A. Kirrander, M. S. Child, and A. V. Stoliarov, Ab initio and quantum-defect calculations for the rydberg states of ArH, *Phys. Chem. Chem. Phys.* **8**, 247 (2006).
- [30] P. Knowles and H.-J. Werner, Internally contracted multiconfiguration-reference configuration interaction calculations for excited states, *Theor. Chim. Acta* **84**, 95 (1992).
- [31] P. Saxe, B. H. Lengsfeld, R. Martin, and M. Page, MESA (molecular electronic structure applications) (1990).
- [32] G. Theodorakopoulos and I. D. Petsalakis, Rydberg spectra of ArH. boundbound interactions, predissociation, and radiative lifetimes of the Rydberg states, *J. Chem. Phys.* **101**, 194 (1994).
- [33] O. I. Baskakov, S. Civiš, and K. Kawaguchi, High resolution emission fourier transform infrared spectra of the 4p-5s and 5p-6s bands of ArH, *J. Chem. Phys.* **122**, 114314 (2005).
- [34] A. V. Stoliarov and M. S. Child, Theoretical study of the ArH⁺ electronic states, *Phys. Chem. Chem. Phys.* **7**, 2259 (2005).
- [35] J. M. Brown, D. A. Jennings, M. Vanek, L. R. Zink, and K. M. Evenson, The pure rotational spectrum of ArH⁺, *J. Mol. Spectrosc.* **128**, 587 (1988).
- [36] M. Cheng, J. M. Brown, P. Rosmus, R. Linguerra, N. Komaha, and E. G. Myers, Dipole moments and orientation polarizabilities of diatomic molecular ions for precision atomic mass measurement, *Phys. Rev. A* **75**, 012502 (2007).

- [37] J. R. Hamilton, A. Faure, and J. Tennyson, Electron-impact excitation of diatomic hydride cations I. HeH^+ , CH^+ , ArH^+ , *Mon. Not. R. Astron. Soc.* **455**, 3281 (2016).
- [38] S. Novotny, Fragmentation of molecular ions in slow electron collisions, Ph.D. thesis, Ruprecht-Karls-Universität Heidelberg, 2008.
- [39] X. Urbain, D. Bech, J.-P. Van Roy, M. Géléoc, S. J. Weber, A. Huetz, and Y. J. Picard, A zero dead-time multi-particle time and position sensitive detector based on correlation between brightness and amplitude, *Rev. Sci. Instrum.* **86**, 023305 (2015).
- [40] V. Wakelam, E. Herbst, J.-C. Loison, I. W. M. Smith, V. Chandrasekaran, B. Pavone, N. G. Adams, M.-C. Bacchus-Montabonel, A. Bergeat, K. Béroff, V. M. Bierbaum, M. Chabot, A. Dalgarno, E. F. van Dishoeck, A. Faure, W. D. Geppert, D. Gerlich, D. Galli, E. Hébrard, F. Hersant *et al.*, A kinetic database for astrochemistry (KIDA), *Astrophys. J. Suppl. Series* **199**, 21 (2012).